

Extending Quantitative Phase Imaging to Polarization-Sensitive Materials

Arthur Baroni, Virginie Chamard, and Patrick Ferrand^{✉*}

Aix-Marseille Université, CNRS, Centrale Marseille, Institut Fresnel, 13013 Marseille, France



(Received 27 January 2020; revised manuscript received 31 March 2020; accepted 21 April 2020; published 12 May 2020)

State-of-the-art optical microscopy fails to image quantitatively complex anisotropic specimens, which are essential in the life sciences, materials science, and optical engineering. In this context, the recent development of Jones-imaging techniques, such as vectorial ptychography, could open up exciting perspectives provided that the measured Jones maps are fully exploited. Here we present a generalized definition of the isotropic phase in the context of arbitrary Jones matrices. We show how to deduce, from combined knowledge of isotropic and anisotropic properties, the underlying structure of the specimen. The power of the method is confirmed by investigations on a biomineral polycrystalline oyster-shell specimen, where we are able to map variations of the three-dimensional orientation of the crystal axis and to highlight structural defects in depth.

DOI: [10.1103/PhysRevApplied.13.054028](https://doi.org/10.1103/PhysRevApplied.13.054028)

I. INTRODUCTION

A wide range of materials exhibit optical anisotropy [1] as a result of their specific crystal structure, molecular order, artificial structuration, or response to induced constraints. Detailed knowledge of these material properties is crucial in several scientific areas, including mineralogy [2], biomineralogy [3], material processing [4], optical engineering [5–7], and cell biology [8].

Dedicated optical microscopy methods have been developed to image specifically these anisotropic properties. One example is polarization microscopy, which consists in analyzing the apparent hue of a specimen placed between crossed polarizers so as to quantify its birefringence [2]. This approach, used for a long time by mineralogists, was subsequently largely perfected in automated forms by use of different modalities involving, for example, fast polarization modulators [9] or spectral-domain encoding [10]. All these methods make it possible to map anisotropic properties such as neutral-axis orientation and retardance with great accuracy. However, polarization microscopy, as most optical imaging methods, is insensitive to the global isotropic phase delay induced by the specimen, which is critical information. For instance, an emblematic frustrating consequence of this limitation is that isotropic matter is indistinguishable from the absence of matter.

On the other hand, quantitative-phase-imaging microscopy, which uses the phase delay for imaging purposes, is a recent and active research field. Various approaches have been developed, including defocusing [11], holography [12], wave-front sensing [13], and ptychography [14].

The capability to provide phase maps offers opportunities, including label-free investigations of biological cells for dry-mass quantification [15,16] or medical diagnosis [12], and the local measurement of temperature in nanostructures [17]. However, because of their polarization-insensitive light-matter interaction model, these methods are inherently designed to address isotropic materials only. For this reason, attempts to investigate anisotropic matter with quantitative phase imaging so far have been restricted to specimens possessing weak retardances [18] or known orientations [19].

Thus, investigating quantitatively anisotropic matter in microscopy requires (i) considering both the isotropic (phase delay, absorption) and the anisotropic (retardance, diattenuation) properties of matter and (ii) accounting for the vectorial nature of light. These requirements are met only by the Jones formalism [20], which is powerful and flexible for optical function calculus but which was not developed for experimental measurements [21].

For this latter reason, so-called Jones microscopy methods were experimentally demonstrated only recently by means of interferometric [22–27] or ptychographic [28] approaches. Moreover, they have provided the raw Jones-matrix maps only as final results or have been restricted to the analysis of simple cases. Thus, data provided by Jones microscopy are greatly underexploited.

In this work we propose a comprehensive theoretical framework aiming at extracting at an ultimate level the optical information contained in Jones-matrix maps obtained experimentally. First, we recall the approach of polar decomposition and introduce a generalized definition of the isotropic phase in the context of arbitrary Jones matrices. Then we show how to infer the underlying

*patrick.ferrand@fresnel.fr

structure of the sample from combined knowledge of the isotropic and anisotropic properties. Finally, the power of this approach is confirmed by investigations conducted on a biomineral polycrystalline specimen.

II. RESULTS

In an anisotropic medium, the propagation of light depends on its state of polarization. This specificity requires light to be modeled by a so-called Jones vector, while the optical properties of matter are locally quantified by a 2×2 complex matrix, the Jones matrix, under the two-dimensional assumption of normal incidence on a flat specimen. This matrix can be written at any point of the object in the general form [20]

$$\mathbf{J} = \begin{pmatrix} J_{xx} & J_{yx} \\ J_{xy} & J_{yy} \end{pmatrix}. \quad (1)$$

The common use of the Jones formalism involves standard Jones matrices, whose multiplications allow one to easily predict the behavior of optical components built with known elements assembled in stacks. The ambition of Jones imaging, on the other hand, is to solve the inverse problem; that is, to deduce, from a given Jones matrix, relevant optical parameters.

If $J_{xy} = J_{yx}$, one can show that Eq. (1) can be reduced to the generic form of a matrix product, where parameters such as the global isotropic phase are usually dropped:

$$\mathbf{J} \propto \mathbf{R}_\theta \begin{pmatrix} 1 & 0 \\ 0 & \gamma \exp(i\Delta\phi) \end{pmatrix} \mathbf{R}_{-\theta}, \quad (2)$$

where \mathbf{R}_θ is a θ -angle rotation matrix [20]. In this common case, Eq. (2) allows one to model the material investigated as uniaxial with retardance $\Delta\phi$, oriented with an angle θ between the fast axis and the current observation frame, and with a diattenuation given by $D = (1 - \gamma^2)/(1 + \gamma^2)$ [8,29].

If $J_{xy} \neq J_{yx}$, this latter simple model is no longer valid, and more-complex arrangements, including stacks of misaligned layers or rotatory-power effects, must be invoked. Despite equivalence theorems [30], extraction of explicitly physical parameters from such Jones matrices remains challenging and can be performed only with appropriate matrix decompositions. In the following, we use the generalized approach introduced by Lu and Chipman [31] based on (i) the polar decomposition

$$\mathbf{J} = \mathbf{J}_R \mathbf{J}_D, \quad (3)$$

where \mathbf{J}_R and \mathbf{J}_D are unitary and non-negative definite Hermitian matrices, respectively, and (ii) the study of the eigenpolarizations of \mathbf{J} .

We propose to identify them as \mathbf{E}_{fast} and \mathbf{E}_{slow} , with

$$\mathbf{J}\mathbf{E}_{\text{fast}} = \xi_{\text{fast}}\mathbf{E}_{\text{fast}}, \quad (4)$$

$$\mathbf{J}\mathbf{E}_{\text{slow}} = \xi_{\text{slow}}\mathbf{E}_{\text{slow}}, \quad (5)$$

where ξ_{fast} and ξ_{slow} are the corresponding complex eigenvalues. Here we choose the terms “fast” and “slow” in such a way that the retardance $\Delta\phi$ obeys

$$0 \leq \Delta\phi = \arg \xi_{\text{slow}} \xi_{\text{fast}}^* \leq \pi, \quad (6)$$

where \star stands for the complex conjugate. This allows us to define a global isotropic phase as

$$\phi = \arg \xi_{\text{fast}} \quad (7)$$

in the case of a positive uniaxial material and

$$\phi = \arg \xi_{\text{slow}} \quad (8)$$

in the case of a negative uniaxial material.

We generalize the above-mentioned fast-axis orientation θ as the orientation of the major axis of the fast eigenpolarization \mathbf{E}_{fast} , calculated directly from its time evolution and report the respective ellipticities (ϵ_{fast} , ϵ_{slow}) calculated from both eigenpolarizations [1]. Finally, we recall that the orthogonality of the eigenpolarizations is quantified by the so-called inhomogeneity η [31], a parameter defined by

$$\eta = |\mathbf{E}_{\text{fast}}^\dagger \cdot \mathbf{E}_{\text{slow}}|, \quad (9)$$

where \dagger stands for the transpose complex conjugate.

Absorption properties are deduced from the matrix \mathbf{J}_D , leading to the extraction of the global transmittance $T = \frac{1}{2}(T_{\text{max}} + T_{\text{min}})$ and the diattenuation D , defined as

$$D = \frac{T_{\text{max}} - T_{\text{min}}}{T_{\text{max}} + T_{\text{min}}}, \quad (10)$$

where T_{max} and T_{min} are the maximum and minimum transmittance, respectively [31]. In strongly diattenuating materials, such as polarizers, the eigenpolarization analysis of \mathbf{J}_D also provides relevant parameters [31], similarly to the analysis of \mathbf{J} reported above. Because such effects are rather rare and not present in the experimental results reported in this work, they will not be discussed here.

In this section, we show how the simultaneous measurement of both isotropic and anisotropic optical parameters, which is a major added value provided by Jones imaging, allows deeper structural knowledge of the specimen investigated, under some assumptions that are clearly specified.

The measured global phase shift ϕ can be written as

$$\phi = \frac{2\pi}{\lambda} \Lambda + C \pmod{2\pi}, \quad (11)$$

where C is an arbitrary constant, λ is the wavelength in vacuum, and the optical path length Λ in a medium of ordinary index n_o and thickness d is given by

$$\Lambda = n_o d. \quad (12)$$

Therefore, in a given measured map of ϕ , if the phase offset C can be determined (e.g., by comparison with an area of reference) and if the sampling of ϕ allows a phase-unwrapping algorithm to be run, then

$$\phi_u = \frac{2\pi}{\lambda} \Lambda = \frac{2\pi}{\lambda} n_o d, \quad (13)$$

where ϕ_u refers to the unwrapped map of $\phi - C$.

The definition of Eq. (6) implies that the measured retardance $\Delta\phi$ is related to the effective birefringence Δn_{eff} , in a single-layer approximation, by

$$\Delta\phi = \left| \arg \left[\exp \left(i \frac{2\pi}{\lambda} \Delta n_{\text{eff}} d \right) \right] \right|, \quad (14)$$

which emphasizes formally the inherent underdetermination of the method. Therefore, if one can assume a zero-order retardance (i.e., $|\Delta n_{\text{eff}}|d < \lambda/2$), then

$$\Delta\phi = \frac{2\pi}{\lambda} |\Delta n_{\text{eff}}| d. \quad (15)$$

Here the birefringence is denoted as “effective” to take into account its dependence on the orientation of the incident light with respect to the index ellipsoid of the material. As a consequence, with the assumptions listed above, the angle β between the so-called optic axis and the incident light is given in an uniaxial material by [1]

$$\beta = \arccos \left[\left(\frac{1/(n_o + \Delta n_{\text{eff}})^2 - 1/n_e^2}{1/n_o^2 - 1/n_e^2} \right)^{1/2} \right], \quad (16)$$

where n_e is the extraordinary index. Finally, one can show that in the case of a negative uniaxial material, the fast-axis orientation θ provides the projected direction of the optic axis in the observation plane. In the case of a positive uniaxial material, the fast-axis orientation θ is at 90° to the projected direction of the optic axis.

In a nutshell, simultaneous knowledge of ϕ and $\Delta\phi$ allows one to measure the three-dimensional orientation of anisotropic matter, this information being integrated over the whole thickness of the material. Equations (13), (15) and (16) apply only if all corresponding conditions are fulfilled: namely, knowledge of the class of anisotropic

		Without diattenuation $D=0$	With diattenuation $D>0$
(a) Isotropic layer		Degenerate	Not applicable
(b) Partial polarizer		Not applicable	
(c) Single retarding layer			
(d) Two or more aligned retarding layers			
(e) Two or more misaligned retarding layers			
(f) Retarding and rotating layers			
(g) Rotating layer			Not applicable

FIG. 1. Summary of the resulting eigenpolarizations for different structural cases, including single or stacked layers (the dashed line represents an anisotropy direction), with and without diattenuation.

material (uniaxial), its corresponding indices, and the zero-order nature of its retardance. In practice, this corresponds to the investigation of identified materials of roughly known thicknesses.

Remarkably, a powerful way to analyze this large number of optical parameters is to investigate the resulting eigenpolarizations for each measured pixel. This allows one, at a single glance, to deduce pixel-wise structural insights as well as global trends. Figure 1 illustrates different physical cases on the basis of their eigenpolarization. Orthogonal linear eigenpolarizations can be attributed to single layers or aligned stackings [Figs. 1(b)–1(d)], whose Jones matrix is written according Eq. (2). Less common is the case of elliptical eigenpolarizations, which open several possibilities of interpretation, including a stacking of two or more birefringent layers oriented differently [Fig. 1(e)] or a combination of layers combining retardance and properties of rotatory power [Fig. 1(f)]. Circular eigenpolarizations are the extreme case, corresponding to the presence of rotatory power only [Fig. 1(g)]. Diattenuation ($D > 0$, right column in Fig. 1) affects the orthogonality of the eigenpolarizations only if they are elliptical [Figs. 1(e) and 1(f)].

III. EXPERIMENTS

To confirm the power of the method, we address the case of a demanding specimen combining a complex structure and a significant anisotropy. Here we investigate a specimen of juvenile *Pinctada margaritifera* oyster shell, whose so-called prismatic layer is made of a unique layer

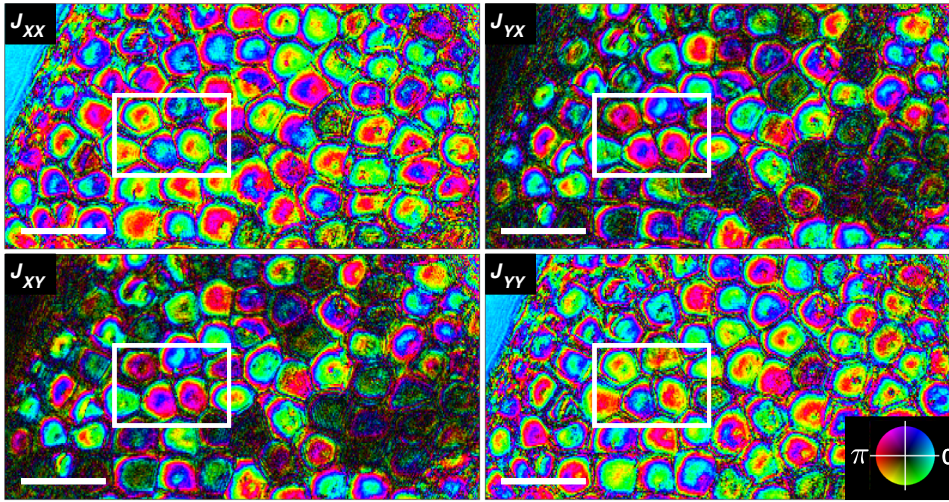


FIG. 2. Experimental Jones-matrix maps of a biomineral specimen as retrieved by vectorial ptychography. The inset shows the complex-value color coding, with phase encoded as hue and modulus encoded as brightness. The rectangle indicates the region of interest analyzed in Fig. 3. The scale bars are $50 \mu\text{m}$.

of single-crystal calcite prisms of size ranging between 10 and $30 \mu\text{m}$ separated by organic walls [3]. Calcite is a negative uniaxial material, so the data analysis in the following is performed accordingly.

Jones imaging is performed by means of vectorial ptychography [32] with the custom setup described in Ref. [28] using a $20\times$ objective (ACHN-P, NA 0.4, Olympus) for collection. The specimen is scanned under $100\text{-}\mu\text{m}$ -effective-diameter illumination probes at wavelength $\lambda = 635 \text{ nm}$ linearly polarized at angles of 0° , 45° , and 90° in the object plane sequentially. The scanning grid contains 270 points with average steps of $9 \mu\text{m}$ along the two scanning directions, with additional random step fluctuations of $\pm 50\%$ to avoid periodic reconstruction ambiguities [33]. Polarization analyses are performed at angles of 0° , 45° , and 90° . Object reconstructions are performed by means of 500 iterations of a conjugate-gradient algorithm allowing the joint estimation of the three probes together with the Jones maps of the object [33]. The reconstructed pixel size is about $0.73 \times 0.97 \mu\text{m}^2$.

A region of $300 \times 150 \mu\text{m}^2$ located at the border of a shell is investigated, and the corresponding Jones maps are reported in Fig. 2. All maps show clearly the morphology of the specimen: namely, a juxtaposition of rounded polygonal elements, corresponding to the calcite prisms. The nonzero values in the off-diagonal maps J_{yx} and J_{xy} evidence the anisotropic nature of the material. The upper-left region is free of the specimen and predictably appears optically isotropic ($J_{xx} = J_{yy}$ and $J_{yx} = J_{xy} = 0$).

IV. DISCUSSION

In the following, for readability, we focus our discussion on a region of interest of $70 \times 50 \mu\text{m}^2$. An overview of the optical and structural parameters of the region-of-interest prisms as retrieved from the Jones maps by the method described in Sec. II is shown in Fig. 3. The

transmittance maps [Fig. 3(a)] confirm observations in white-light transmission microscopy; namely, rather transparent prisms separated by opaque walls. The phase map [Fig. 3(b)] reveals clear local variations for each prism on the order of 3 rad, corresponding to typical differences of thickness of 200 nm between the center and the border [Eq. (11)], with a domelike profile. Prism 2 shows local phase jumps of π , inherently due to a swap of ξ_{slow} and ξ_{fast} in Eqs. (6)–(8), when the value of $\Delta\phi$ reaches π , which is the upper limit of a zero-order retardance. The map of the optical path length, which is obtained after the unwrapping of ϕ [34] and shown in Fig. 3(c), quantifies the prism thicknesses, showing an assembly in terracelike levels, growing from left to right. In spite of the domelike profile accurately quantified and discussed above, each prism appears to be rather flat in regard of its typical lateral extent of $20 \mu\text{m}$ and thickness ($1\text{--}3 \mu\text{m}$).

Retardance [Fig. 3(d)] and fast-axis-orientation θ [Fig. 3(e)] maps show rather homogeneous values within a prism, with possible variations from one prism to the next. Here θ indicates directly the projected direction of the optic axis of the material, except in some regions of prism 2, where the zero-order condition is not fulfilled, as discussed above. The diattenuation D [Fig. 3(f)] shows high values near the inhomogeneous interfaces of the prisms, most likely because light propagates here at oblique incidence with respect to the steep prism border, thus experiencing polarization-sensitive Fresnel transmission coefficients [1]. The diattenuation is weak within prisms, except at very localized areas, indicated by arrows in Figs. 3(f)–3(h), which will be discussed further. Inhomogeneity η [Fig. 3(g)] and average ellipticity $\epsilon = \frac{1}{2}(\epsilon_{\text{fast}} + \epsilon_{\text{slow}})$ [Fig. 3(h)] show similar behaviors for the same geometrical reasons.

Correlative knowledge of both OPL and $\Delta\phi$ maps allows us to deduce the tilt angle β of the optic axis, according to Eq. (16), corresponding in this case to the crystallographic c axis of the crystalline calcite material.

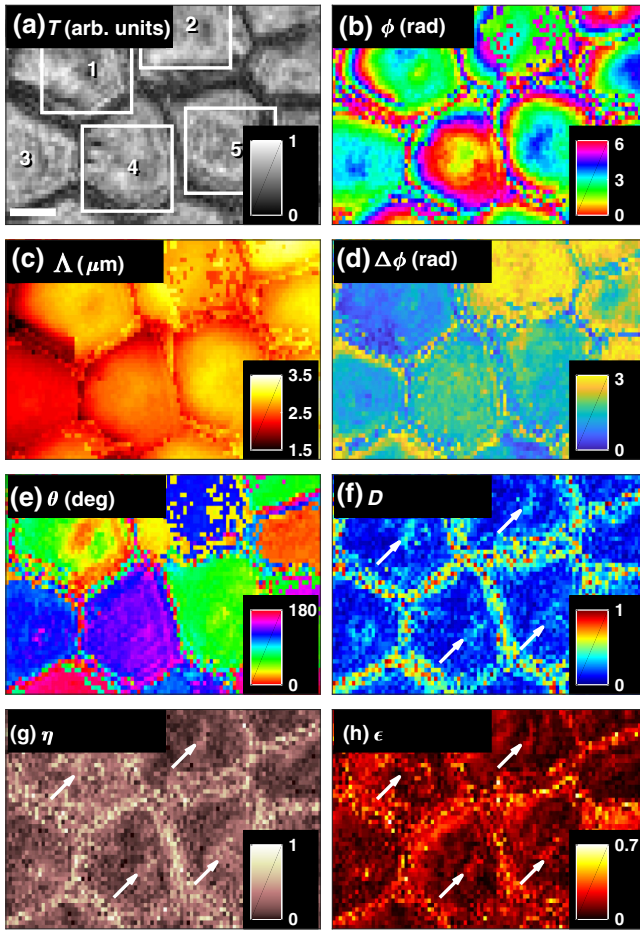


FIG. 3. Optical and structural properties retrieved from the framed area of the Jones maps in Fig. 2. The scale bar is $10 \mu\text{m}$.

Combining the map of β with the maps of θ [Fig. 3(e)] allows us to map the three-dimensional orientation of the c axis at microscopic resolution, as shown in Fig. 4. Remarkably, the variations of retardance between prisms [which are emphasized in Fig. 3(d)] are mainly due to variations of the c -axis tilt angle. This tilt angle is rather homogeneous in each individual prism, in agreement with the crystalline nature of the material. Prisms 3–5 show a rather high uniformity of θ within each prism. Following closely the variations of the retardance [Fig. 3(d)], the tilt angle β appears very uniform, but to a lesser extent in prisms 3 and 5. Prism 1 possesses a c axis that is almost perpendicular to the specimen plane (i.e., almost along the direction of observation), with β ranging between 0° and 30° , and θ ranging between 0° and 90° in a wavy fashion, suggesting a continuous deformation of the crystal structure over the prism.

To discuss further the underlying structural properties of the prisms, we display in Fig. 5 an enlargement for four of them [areas framed in Fig. 3(a)] in a map of the ellipticity ϵ , on top of which we draw, for each pixel,

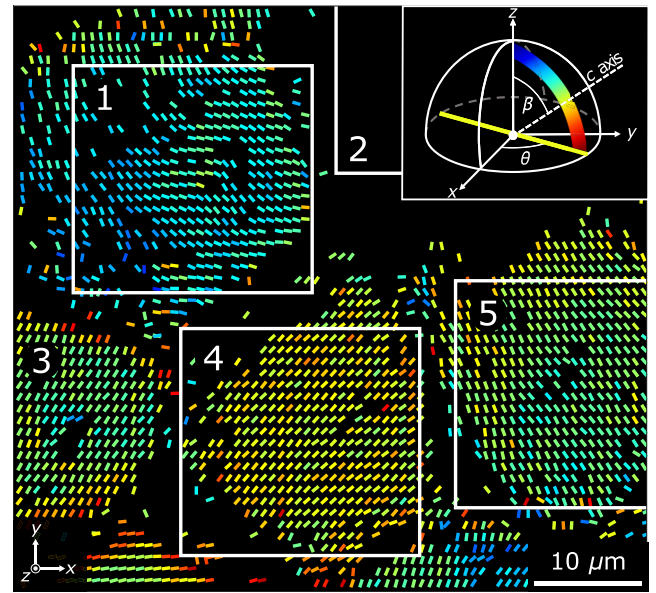


FIG. 4. Orientation of the c axis of the calcite in the sample depicted with β (tilt angle) and θ (projected angle in the plane) for prisms 1, 3, 4, and 5 as framed in Fig. 3(a). Data for prism 2 are not processed due to the uncertainty introduced by the unwrapping algorithm on the optical path length, which could induce a bias on β . Data corresponding to areas where $\epsilon > 0.2$ [see Fig. 3(h)] do not fulfill the single-layer condition and are not processed. At each pixel the stick is oriented according to θ , while its color encodes the value of β (see the inset). The scale bar is $10 \mu\text{m}$.

the local eigenpolarizations. For all observed prisms, two different areas can be distinguished on the basis of their eigenpolarizations.

Low-ellipticity areas (dark in Fig. 5) appear in most of every prism, and correspond to linear eigenpolarizations. As discussed previously (see Fig. 1), these regions are made of aligned layers of anisotropic material, most probably a unique layer of crystalline calcite in our case.

High-ellipticity areas, appearing bright, are mostly confined at the border of the prisms and to a central crescent-like localized area. These areas are also characterized by inhomogeneous eigenpolarizations ($\eta > 0$), corresponding to Figs. 1(e) and 1(f). From the general properties of calcite, (i.e., no rotatory power), these features are the unambiguous signature of a material made of optically anisotropic layers misaligned in depth. As explained for Fig. 3(f), the slope in the prism geometry induces diattenuation, whose axes do not necessarily match the projected c axis of the material, yielding an optical behavior of two misaligned anisotropic layers. If this interpretation can be given at the prism border, where the optical path length varies [Fig. 3(c)], it cannot be invoked at the central high-ellipticity area, where the optical path length is almost constant. These observations suggest that the prisms possess,

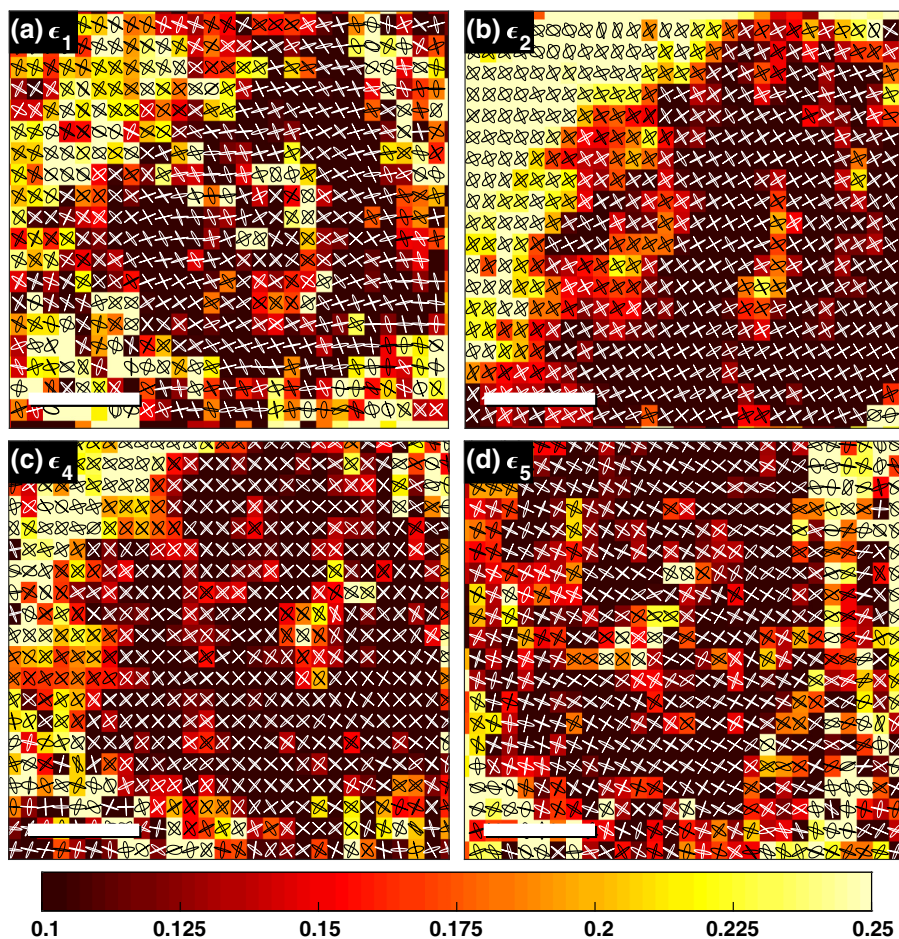


FIG. 5. Enlargements of the ellipticity map ϵ , on top of which is drawn, for each pixel, the corresponding eigenpolarizations for the areas 1, 2, 4, and 5 as framed in Fig. 4. The ellipse plotting color changes from black to white for better readability. The scale bars are $5 \mu\text{m}$.

near their center, a structural singularity, which is likely associated with the biomineralization process [35].

V. CONCLUSION

In conclusion we demonstrate theoretically and experimentally a method to perform quantitative structural microscopy on demanding anisotropic materials. This is done through the exhaustive analysis of experimental Jones-matrix maps, after the introduction of a generalized definition of the isotropic global phase. The power of the method is illustrated on a biomineral specimen of juvenile *Pinctada margaritifera* oyster shell by means of vectorial ptychography. The correlation of the extracted quantitative maps of the optical properties leads to precise structural information, such as the three-dimensional orientation of the c axis of the crystalline calcite, and evidences for structural defects in depth, mapped over a wide field of view, at optical microscopy resolution. This method opens alternative imaging perspectives for understanding complex anisotropic specimens, which are essential in the life sciences, materials science, and optical engineering.

ACKNOWLEDGMENTS

We are grateful to Miguel A. Alonso for valuable advice. Gilles Le Moullac and Denis Saulnier from Ifremer (Ressources Marines en Polynésie Française) are warmly acknowledged for providing the specimen of *Pinctada margaritifera* shell. This work received funding from the European Research Council under the European Union's Horizon 2020 research and innovation program (Grant No. 724881).

-
- [1] M. Born, E. Wolf, A. B. Bhatia, P. C. Clemmow, D. Gabor, A. R. Stokes, A. M. Taylor, P. A. Wayman, and W. L. Wilcock, *Principles of Optics: Electromagnetic Theory of Propagation, Interference and Diffraction of Light* (Cambridge University Press, Cambridge, New York, 1999), 7th ed.
 - [2] R. E. Stoiber and S. A. Morse, *Crystal Identification with the Polarizing Microscope* (Springer US, Boston, MA, 1994).
 - [3] Y. Dauphin, E. Zolotoyabko, A. Berner, E. Lakin, C. Rollion-Bard, J. P. Cuif, and P. Fratzl, Breaking the long-standing morphological paradigm: Individual prisms in

- the pearl oyster shell grow perpendicular to the c-axis of calcite, *J. Struct. Biol.* **205**, 121 (2019).
- [4] K. Milenko, S. Pissadakis, G. Gkantzounis, A. Aluculesi, and G. Fytas, Probing stress-induced optical birefringence of glassy polymers by whispering gallery modes light localization, *ACS Omega* **2**, 9127 (2017).
- [5] R. A. Chipman, W. S. T. Lam, G. Young, W. S. T. Lam, and G. Young, *Polarized Light and Optical Systems* (CRC Press, Boca Raton, 2018).
- [6] S. Sivankutty, E. R. Andresen, G. Bouwmans, T. G. Brown, M. A. Alonso, and H. Rigneault, Single-shot polarimetry imaging of multicore fiber, *Opt. Lett.* **41**, 2105 (2016).
- [7] J. P. Balthasar Mueller, N. A. Rubin, R. C. Devlin, B. Groever, and F. Capasso, Metasurface Polarization Optics: Independent Phase Control of Arbitrary Orthogonal States of Polarization, *Phys. Rev. Lett.* **118**, 113901 (2017).
- [8] S. B. Mehta, M. Shribak, and R. Oldenbourg, Polarized light imaging of birefringence and diattenuation at high resolution and high sensitivity, *J. Opt.* **15**, 094007 (2013).
- [9] R. Oldenbourg and G. Mei, New polarized light microscope with precision universal compensator, *J. Microsc.* **180**, 140 (1995).
- [10] A. L. Gratiot, M. Dubreuil, S. Rivet, and Y. Le Grand, Scanning Mueller polarimetric microscopy, *Opt. Lett.* **41**, 4336 (2016).
- [11] A. Barty, K. A. Nugent, D. Paganin, and A. Roberts, Quantitative optical phase microscopy, *Opt. Lett.* **23**, 817 (1998).
- [12] Y. Park, C. Depeursinge, and G. Popescu, Quantitative phase imaging in biomedicine, *Nat. Photonics* **12**, 578 (2018).
- [13] P. Bon, G. Maucort, B. Wattellier, and S. Monneret, Quadriwave lateral shearing interferometry for quantitative phase microscopy of living cells, *Opt. Express* **17**, 13080 (2009).
- [14] R. Kasprowicz, R. Suman, and P. O'Toole, Characterising live cell behaviour: Traditional label-free and quantitative phase imaging approaches, *Int. J. Biochem. Cell. Biol.* **84**, 89 (2017).
- [15] J. Marrison, L. Rätty, P. Marriott, and P. O'Toole, Ptychography – a label free, high-contrast imaging technique for live cells using quantitative phase information, *Sci. Rep.* **3**, 2369 (2013).
- [16] S. Aknoun, J. Savatier, P. Bon, F. Galland, L. Abdeladim, B. F. Wattellier, and S. Monneret, Living cell dry mass measurement using quantitative phase imaging with quadriwave lateral shearing interferometry: An accuracy and sensitivity discussion, *J. Biomed. Opt.* **20**, 126009 (2015).
- [17] G. Baffou, P. Bon, J. Savatier, J. Polleux, M. Zhu, M. Merlin, H. Rigneault, and S. Monneret, Thermal imaging of nanostructures by quantitative optical phase analysis, *ACS Nano* **6**, 2452 (2012).
- [18] S. Aknoun, P. Bon, J. Savatier, B. Wattellier, and S. Monneret, Quantitative retardance imaging of biological samples using quadriwave lateral shearing interferometry, *Opt. Express* **23**, 16383 (2015).
- [19] N. M. Dragomir, X. M. Goh, C. L. Curl, L. M. D. Delbridge, and A. Roberts, Quantitative polarized phase microscopy for birefringence imaging, *Opt. Express* **15**, 17690 (2007).
- [20] R. C. Jones, A new calculus formalism for the treatment of optical systems. I. Description and discussion of the method, *J. Opt. Soc. Am.* **31**, 488 (1941).
- [21] E. Collett, *Polarized Light. Fundamentals and Applications* (Marcel Dekker, New York, 1993).
- [22] S. Yoneyama, Y. Morimoto, and M. Kawamura, Two-dimensional stress separation using phase-stepping interferometric photoelasticity, *Meas. Sci. Technol.* **16**, 1329 (2005).
- [23] S. Makita, Y. Yasuno, T. Endo, M. Itoh, and T. Yatagai, Jones matrix imaging of biological samples using parallel-detecting polarization-sensitive fourier domain optical coherence tomography, *Opt. Rev.* **12**, 146 (2005).
- [24] T. Colomb, F. Dürr, E. Cuche, P. Marquet, H. G. Limberger, R.-P. Salathé, and C. Depeursinge, Polarization microscopy by use of digital holography: Application to optical-fiber birefringence measurements, *Appl. Opt.* **44**, 4461 (2005).
- [25] Z. Wang, L. J. Millet, M. U. Gillette, and G. Popescu, Jones phase microscopy of transparent and anisotropic samples, *Opt. Lett.* **33**, 1270 (2008).
- [26] Y. Kim, J. Jeong, J. Jang, M. W. Kim, and Y. Park, Polarization holographic microscopy for extracting spatio-temporally resolved Jones matrix, *Opt. Express* **20**, 9948 (2012).
- [27] S. Shin, K. Lee, Z. Yaqoob, P. T. C. So, and Y. Park, Reference-free polarization-sensitive quantitative phase imaging using single-point optical phase conjugation, *Opt. Express* **26**, 26858 (2018).
- [28] P. Ferrand, A. Baroni, M. Allain, and V. Chamard, Quantitative imaging of anisotropic material properties with vectorial ptychography, *Opt. Lett.* **43**, 763 (2018).
- [29] M. Menzel, K. Michielsen, H. De Raedt, J. Reckfort, K. Amunts, and M. Axer, A Jones matrix formalism for simulating three-dimensional polarized light imaging of brain tissue, *J. R. Soc. Interface* **12**, 20150734 (2015).
- [30] H. Hurwitz and R. C. Jones, A new calculus formalism for the treatment of optical systems. II. Proof of the three equivalence theorems, *J. Opt. Soc. Am.* **31**, 493 (1941).
- [31] S.-Y. Lu and R. A. Chipman, Homogeneous and inhomogeneous Jones matrices, *J. Opt. Soc. Am. A* **11**, 766 (1994).
- [32] P. Ferrand, M. Allain, and V. Chamard, Ptychography in anisotropic media, *Opt. Lett.* **40**, 5144 (2015).
- [33] A. Baroni, M. Allain, P. Li, V. Chamard, and P. Ferrand, Joint estimation of object and probes in vectorial ptychography, *Opt. Express* **27**, 8143 (2019).
- [34] J. M. Bioucas-Dias and G. Valadao, Phase unwrapping via graph cuts, *IEEE Trans. Image Process.* **16**, 698 (2007).
- [35] J.-P. Cuif, M. Burghammer, V. Chamard, Y. Dauphin, P. Godard, G. L. Moullac, G. Nehrke, and A. Perez-Huerta, Evidence of a biological control over origin, growth and end of the calcite prisms in the shells of *Pinctada margaritifera* (pelecypod, pterioidea), *Minerals* **4**, 815 (2014).